Original Research Article

Demonstration of interferometric properties of unbalanced Mach-Zehnder Interferometer

ABSTRACT

This article presents a demonstration of the interferometric characteristics inherent in an unbalanced Mach-Zehnder Interferometer (MZI), implemented on a silicon-on-insulator platform through precision fabrication techniques. The investigation delves into the intricate relationship between the free spectral range (FSR) and various lengths of unbalanced MZIs. Notably, a comparison between simulation and experimental outcomes reveals a remarkable agreement.

Keywords: Mach-Zehnder Interferometer, photonics, silicon-on-insulator, waveguides

1. INTRODUCTION

Silicon photonics devices have become increasingly popular due to their appealing properties. The small size, large refractive index contrast and CMOS compatibility are among the properties of silicon photonic devices that make it a choice device in several industries - telecommunication, biomedical, etc.[1], [2]. One of the most widely used silicon photonic device components is the Mach-Zehnder interferometer (MZI). The Mach-Zehnder Interferometer implemented on a silicon platform stands out as a pivotal element for various applications, ranging from telecommunications (used in photonic waveguide switches, and photonic modulators) to sensing, neural networks, quantum and signal processing [3], [4], [5], [6], [7], [8], [9], [10], [11]. The utility of the MZI stems from its interferometric property, and this is achieved by creating a relative phase shift between both arms of the MZI. This phase shift is achieved either using phase shifters or by making the optical path length of both arms of the MZI to be unequal. The MZI configuration where both arms of the MZI are unequal is known as an unbalanced MZI.Unbalanced MZI has been used in displacement sensing[12], gas sensing[13], mode switching[14], and modulation[15].

In this article, we demonstrated an unbalanced MZI design that we modelled, simulated and subsequently fabricated. We examined several unbalanced MZI designs and analyzed the simulation and experimental transmission properties of the devices. We elucidated the process of the waveguide modelling and performed analyses to compensate for fabrication variations and detailed some of the data analyses.

2. MATERIAL AND METHODS

2.1 THEORY

A Mach-Zehnder Interferometer (MZI) comprises a beam splitter and beam combiner, interconnected by a pair of waveguides, as illustrated in Figure 1. The MZI configuration involves the beam splitter dividing incident light at the waveguide input (E_i) into the arms or

branches of the waveguides. Subsequently, the light is recombined at the output by a beam combiner. At the output, the light from both arms of the waveguides interferes to produce an output (E_o). In silicon photonics, a y-splitter and y-combiner are used as the beam splitter and combiner respectively.

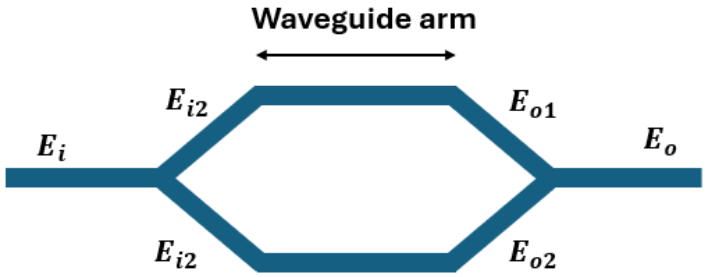

Figure 1. Balanced MZI. Both waveguide arms are equal.

The interference seen at the output can vary depending on the optical path length of the light. If the optical path length in both arms is the same (as in a balanced configuration), the light experiences no phase shift, hence, there is constructive interference at the output. If, however, the phase shift between the light at the branches is π (180°), destructive interference occurs. A phase difference in an MZI can be achieved by varying the optical path length. This can be done using an unbalanced MZI configuration as shown in figure 2; as we see in this case, the length of one of the arms of the MZI is relatively longer.

Now, let us describe the field at the output of the interferometer in Figure 2. To do this, we would consider both halves of the interferometer. At the y-splitter, the light is split equally into the two branches; each of which has an electric field $E_{i1} = E_{i2} = \frac{E_i}{\sqrt{2}}$ with intensity $I_1 = I_2 = \frac{I}{2}$. At the y-combiner, the electric field at the ports are $E_{o1} = \frac{E_{i1}}{\sqrt{2}}$ and $E_{o2} = \frac{E_{i2}}{\sqrt{2}}$ respectively. Finally, at the output, the field is a vector addition of E_{o1} and E_{o2} divide by $\sqrt{2}$, i.e. $E_o = \frac{E_{o1}+E_{o2}}{\sqrt{2}}$

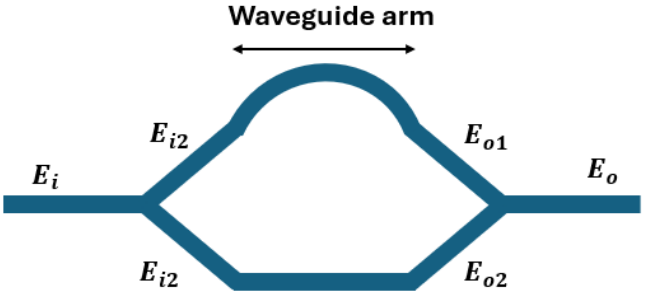

Figure 2. Unbalanced MZI. Both waveguide arms are unequal.

For a plane wave of $E = E_0 e^{i(\omega t - \beta z)}$ with a propagation constant $\beta = \frac{2\pi n}{\lambda}$, we will have that:

$E_{o1} = \frac{E_i}{\sqrt{2}} e^{-i\beta L_1}$ (V/m) (1)

$E_{o2} = \frac{E_i}{\sqrt{2}} e^{-i\beta L_2}$ (V/m) (2)

Therefore, the output at the branch will become:

$E_o = \frac{E_{o1}+E_{o2}}{\sqrt{2}} = \frac{E_i}{\sqrt{2}}(e^{-i\beta L_1} + e^{-i\beta L_2})$ (V/m) (3)

And the intensity is:

$I_o = \frac{I_i}{4}\left[e^{-i\beta L_1} + e^{-i\beta L_2}\right] = \frac{I_i}{2}[1 + \cos(\beta \Delta L)]$ (4)

From Equation 4, we can see the relationship between the optical path difference and the intensity of the light. The optical path difference creates a phase shift in the intensity of the light.

2.2MODELLING AND SIMULATION

2.2.1 Waveguide

In this project, we use a strip waveguide with a 220nm height and a 500nm width. The simulation of the mode profile was carried out using Lumerical mode as shown in figure 3. We similarly obtain the effective and group index dependence on the wavelength as shown in figures 4. We will observe that the effective index decreases with increasing wavelength while the group index increases with increasing wavelength.

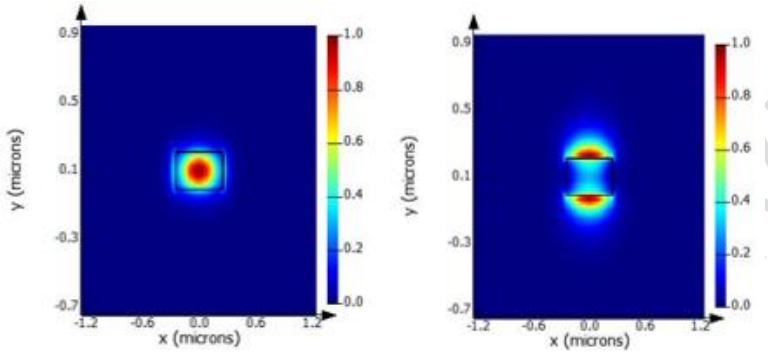

Figure 3. Electric field intensities for TE and TM modes of the waveguide

The compact model of the waveguide used in this simulation is given by Equation 5. It describes the wavelength dependence of the refractive index.

$$n_{eff}(\lambda) = 2.447 - 1.133(\lambda - 1.55) - 0.041(\lambda - 1.55)^2 \quad (5)$$

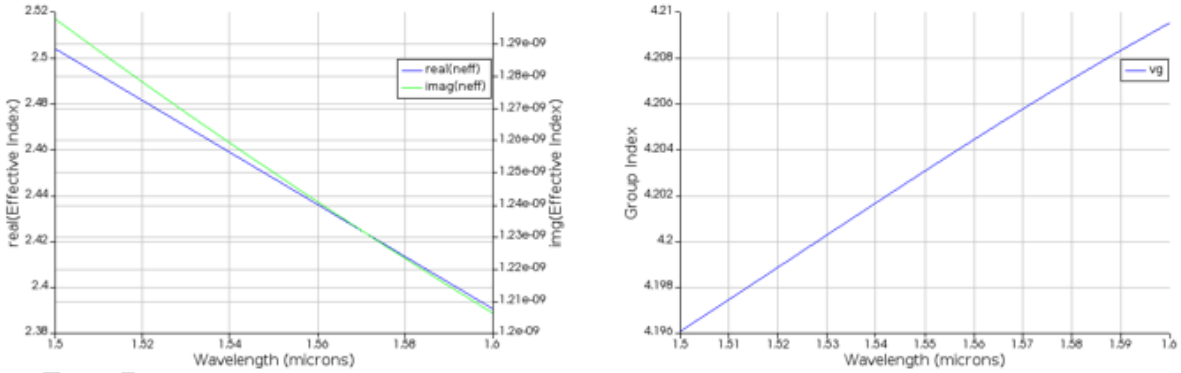

Figure 4.(Left) Wavelength dependence on effective refractive index (Right) Wavelength dependence on group index

2.2.2MZI

The transfer function of the MZI is described in Equation 4. An interferometer is characterized by the free spectral range (FSR) which relates the wavelength of the field to the path length difference in the interferometer. The FSR can be expressed mathematically as

$$FSR = \frac{\lambda^2}{(n_g \Delta L)}(\text{nm}) \quad (6)$$

To demonstrate the interferometric properties of the unbalanced MZI, several MZIs with different optical path differences, ΔL, were designed and simulated. The details of path lengths and the corresponding FSR of the MZIs can be found in Table 1. From the table, we can observe the inverse relationship between the FSR and the optical path difference, as seen in Equation 6. This phenomenon informs the use of MZIs for metrological purposes[13]. The simulation of the devices was done using Lumerical Interconnect software. The MZI configuration used in the simulation is shown in figure 5. As seen in the figure, the input light from the Optical Network Analyzer (ONA_2) is coupled into the input grating coupler (SPAR_4) and then split into the two arms of the waveguides by the input Y-splitter. In the simulation, we set the waveguides (WGD_1 and WGD_2) to have the optical phase differences listed in table 1. The light from both waveguides are combined in the output Y-splitter where they interfere. The output light is coupled into the Optical Network Analyzer using the output grating coupler (SPAR_1).

Table 1. FSR for different lengths

ΔL(μm)	FSR (nm)
0	0
929.77	0.66
303.84	1.99
197.73	3.04
142.87	4.2

The simulation of the output transmission spectrum of the MZI as seen in the optical network analyzer is presented in figure 6.

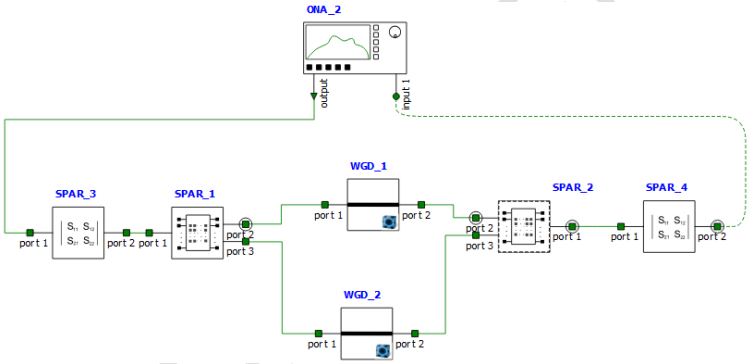

Figure 5. MZI simulation on Lumerical Interconnect. ONA_2 represents the Optical Network Analyzer; SPAR_3 and SPAR_4 are models of grating couplers; SPAR_1 and SPAR_2 are models of Y_splitters and WGD_1 and WGD_2 represents the waveguides in the different arms of the MZI.

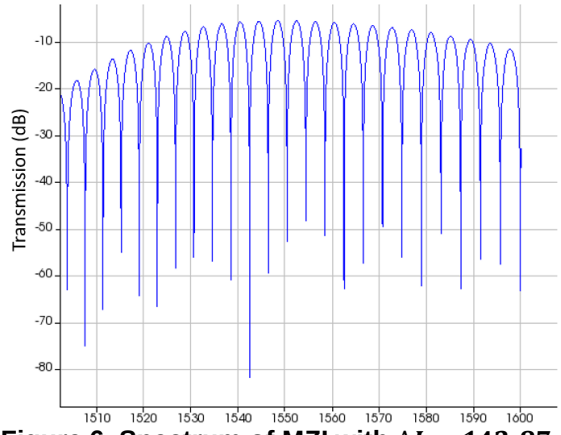

Figure 6. Spectrum of MZI with $\Delta L = 142.87\mu m$ and $FSR = 4.2nm$

2.3 LAYOUT

The layout of the device to be fabricated is shown in figure 7. It contains the different unbalanced MZIs with different optical path lengths.

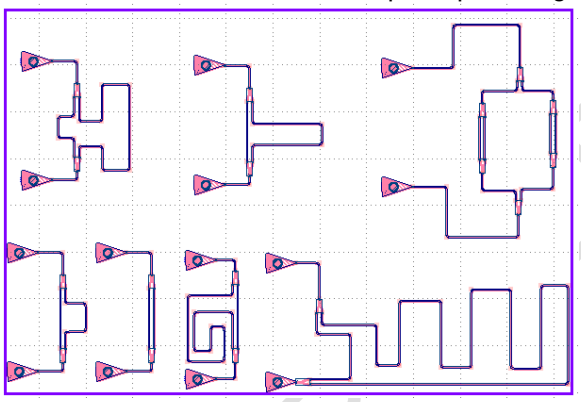

Figure 7. Layout for fabrication

2.4 FABRICATION AND MEASUREMENT

The layout in figure 7 was sent for fabrication at the Washington Nanofabrication Facility (WNF). The devices were fabricated using 100 keV Electron Beam Lithography [16]. The fabrication used a silicon-on-insulator wafer with 220 nm thick silicon on 3 µm thick silicon dioxide. The substrates were 25 mm squares diced from 150 mm wafers.

2.4.1 Manufacturing challenges

There are several challenges of silicon photonics manufacturing that lead to manufacturing variability. This needs to be considered in our simulation to model their impact on the circuit performance. To predict variation in device and circuit performance, we will use the experimental method known as the corner analysis technique which is based on environmental conditions. This technique observes how a desired output varies with the variation of a set of device features. For the strip waveguide, two process variations namely, the height and width were considered, and the desired observed output is the FSR. The nominal design for the waveguide is based on 500nm×200nm. However, we will consider the height and width variation between 215.3-223.1nm and 470-510nm respectively.

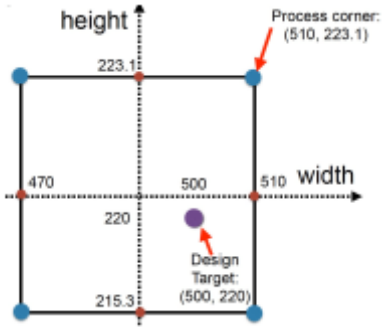

Figure 8: Corner analysis model. This shows the variation of the width and height of the waveguides, up to a certain corner limit.

To consider the identified range variation, we perform the simulation for 8 corners pointed on the diagram. We then show the variation impact on both the effective and group index of the waveguide in Table 2. It is the effective and group index results that are used to obtain the FSR variation.

TABLE 2.Waveguide simulation based on corner analysis

Corner (nm)	Effective Index	Group Index
470 x 215.3	2.433	4.253
470 x 223.1	2.464	4.2612
500 x 220	2.5038	4.2303
500 x 215.3	2.484	4.194
500 x 223.1	2.5145	4.203
510 x 220	2.516	4.187
510 x 215.3	2.497	4.178
510 x 223.1	2.527	4.189

For the different waveguides, we obtain the new FSR given a fabrication variability for the different corners. The result of these variations for the different MZIs with different optical path lengths are detailed in Tables 3 and 4. From the table, we observed that the fabrication variation corresponds to a variation of the FSR between 1.8% to 2.2%. This is not a very consequential variation that can significantly affect our results.

TABLE 3.Variability in FSR for MZI with different optical path length differences

ΔL = 929.77μm		ΔL = 303.84μm		ΔL = 197.73μm	
Corner (nm)	**FSR (nm)**	**Corner (nm)**	**FSR (nm)**	**Corner (nm)**	**FSR (nm)**
470 x 215.3	0.607	470 x 215.3	1.85	470 x 215.3	2.856
470 x 223.1	0.606	470 x 223.1	1.85	470 x 223.1	2.851
500 x 220	0.611	500 x 220	1.86	500 x 220	2.872
500 x 215.3	0.616	500 x 215.3	1.88	500 x 215.3	2.897
500 x 223.1	0.614	500 x 223.1	1.88	500 x 223.1	2.890
510 x 220	0.617	510 x 220	1.88	510 x 220	2.901
510 x 215.3	0.618	510 x 215.3	1.89	510 x 215.3	2.908
510 x 223.1	0.616	510 x 223.1	1.88	510 x 223.1	2.900

TABLE 4.Variability in FSR for MZI with different optical path length differences

ΔL = 142.87µm		ΔL = 32.8µm	
Corner (nm)	**FSR (nm)**	**Corner (nm)**	**FSR (nm)**
470 x 215.3	3.953	470 x 215.3	17.222
470 x 223.1	3.946	470 x 223.1	17.189
500 x 220	3.975	500 x 220	17.314
500 x 215.3	4.009	500 x 215.3	17.464
500 x 223.1	4.000	500 x 223.1	17.427
510 x 220	4.016	510 x 220	17.493
510 x 215.3	4.024	510 x 215.3	17.531
510 x 223.1	4.014	510 x 223.1	17.485

3. RESULTS AND DISCUSSION

3.1 EXPERIMENTAL DATA

After fabrication, the devices were characterized to obtain the experimental data. To characterize the devices, a custom-built automated test setup [17], [18] with automated control software written in Python was used [19]. An Agilent 81600B tunable laser was used as the input source and Agilent 81635A optical power sensors as the output detectors. The wavelength was swept from 1500 to 1600 nm in 10 pm steps. A polarization-maintaining (PM) fibre was used to maintain the polarization state of the light and to couple the TE polarization into the grating couplers [20]. A 90º rotation was used to inject light into the TM grating couplers [20]. A polarization-maintaining fibre array was used to couple light in/out of the chip.

3.2 DATA ANALYSIS

After measurement, we obtain the raw data from all the outputs as shown in figure 9.

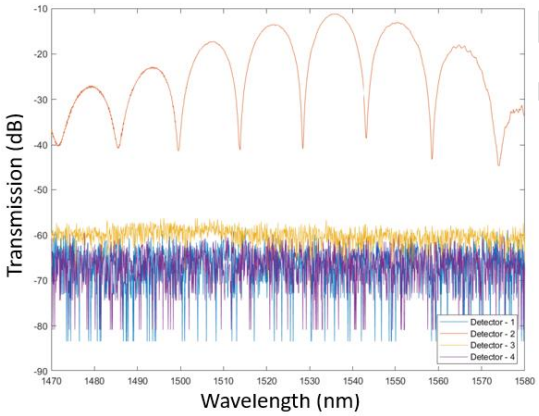

Figure 9. Raw data of MZI with $\Delta L = 32.8\mu m$

We cannot use the raw experimental data as it is not appropriate for data analysis. We need to perform baseline correction and also fit the curve. This was performed for the MZI with $\Delta L = 32.8\mu m$ for clarification. A similar operation is also performed with the other MZIs. The first step was to plot the data and perform a baseline correction as shown in Figure 10b. Afterwards, baseline is fitted to an MZI model starting with initial parameters (Figure 10c) before the final fit is achieved (Figure 10d).

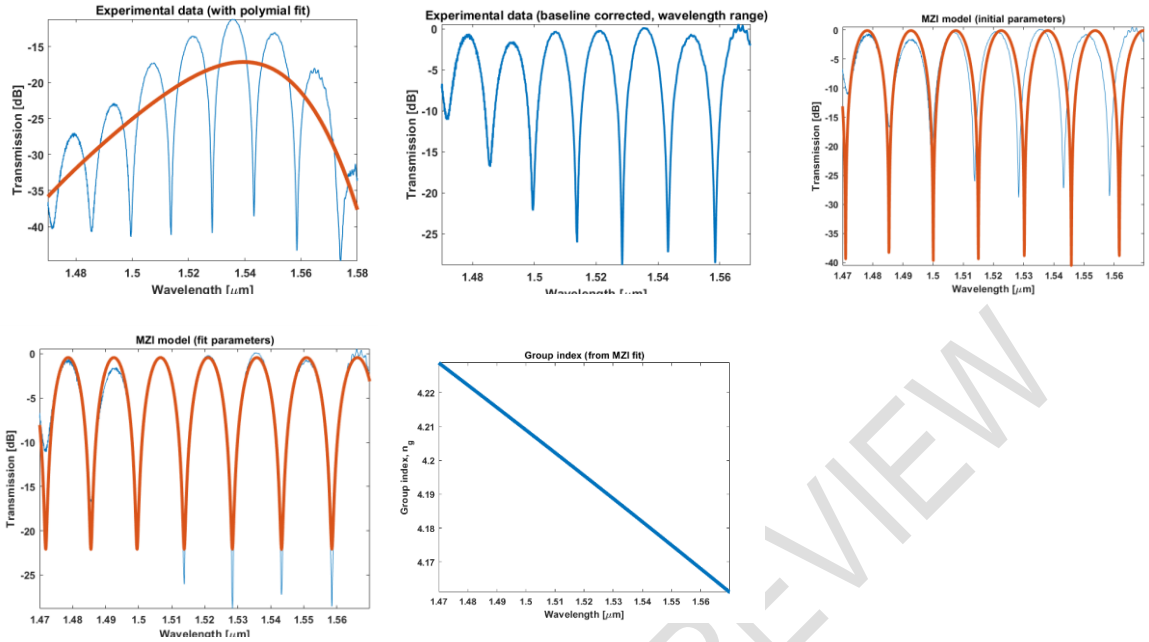

Figure 10. (a) Data before baseline correction (b) Data after baseline correction, (c)-(d) curve fitting, (e) Group index of MZI with $\Delta L = 32.8\mu m$

The transfer functions of the experimental results of the MZIs were plotted as shown in figures 11a and b.

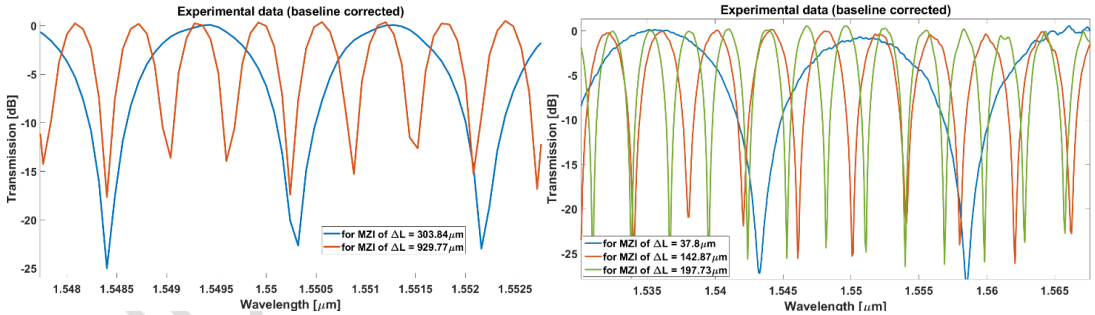

Figure 11. (a) Transfer function of MZI with $\Delta L = 32.8\mu m, 142.87\mu m$&197.73$\mu m$ (b) Transfer function of MZI with $\Delta L = 303.84\mu m$& 929.77μm

3.3 SIMULATION VS EXPERIMENTAL RESULTS

A comparison of the experimental and the fitted simulation results of the MZI are shown in Figures 12 (a) to (e). From the figures, we can observe a varying deviation from the experiment and simulation, and this is expected. The deviation is because the simulation did not take into consideration, factors like incomplete destructive interference at the transmission dips and variation in the waveguide dimensions. This deviation varies depending on the particular MZI. This variation also causes a change in the FSR of the device. What is most important is that the experimental results and the simulation results agree. It should be noted that this study only demonstrates the interferometric properties of unbalanced MZI, a likely further study will benefit from applying this principle in the design of sensors and other devices.

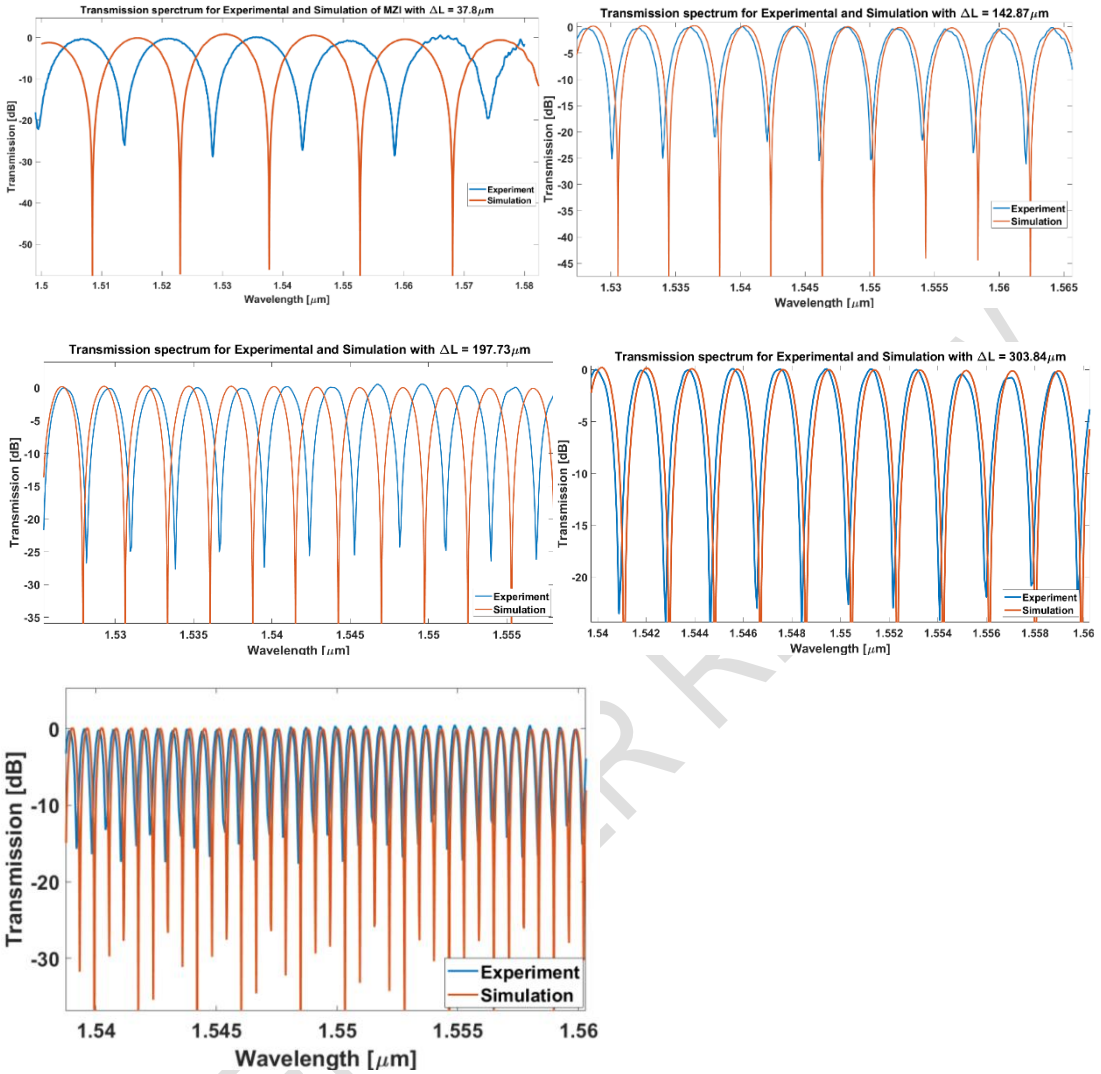

Figure 12. Transmission spectra for experimental and simulation of MZI with length (a) $\Delta L = 32.8\mu m$ (b) $\Delta L = 142.87\mu m$(c)$\Delta L = 197.73\mu m$ (d) $\Delta L = 303.84\mu m$ (e) $\Delta L = 929.77\mu m$

4. CONCLUSION

This article describes the MZI and the waveguide used in the construction of the MZI. We characterized the wavelength dependence of the group and effective indices of the waveguide. We further explained the transfer function and the FSR of the MZI. Finally, we show and compare, the simulation and experimental results of the MZIs of lengths $\mathbf{32.8}\boldsymbol{\mu m}, \mathbf{142.87}\boldsymbol{\mu m}\mathbf{197.73}\boldsymbol{\mu m}, \mathbf{303.84}\boldsymbol{\mu m}$& $929.77\boldsymbol{\mu m}$. The results confirm the variation of the free spectral range due to the phase shift variation for different optical path length difference in MZIs.It is because of the variation of the free spectral range that unbalanced MZI can be used for sensing, switching and modulation.

REFERENCES

[1] L. Pavesi, “Thirty Years in Silicon Photonics: A Personal View,” Front. Phys., vol. 9, p. 786028, Dec. 2021, doi: 10.3389/fphy.2021.786028.

[2] S. Shekhar et al., “Roadmapping the next generation of silicon photonics,” Nat Commun, vol. 15, no. 1, p. 751, Jan. 2024, doi: 10.1038/s41467-024-44750-0.

[3] R. S. El Shamy, M. A. Swillam, M. M. ElRayany, A. Sultan, and X. Li, “Compact Gas Sensor Using Silicon-on-Insulator Loop-Terminated Mach–Zehnder Interferometer,” presented at the Photonics, MDPI, 2021, p. 8.

[4] X. Jiang, Y. Chen, F. Yu, L. Tang, M. Li, and J.-J. He, “High-sensitivity optical biosensor based on cascaded Mach–Zehnder interferometer and ring resonator using Vernier effect,” Optics letters, vol. 39, no. 22, pp. 6363–6366, 2014.

[5] C. A. Millar, D. Harvey, and P. Urquhart, “Fibre reflection mach-zehnder interferometer,” Optics communications, vol. 70, no. 4, pp. 304–308, 1989.

[6] F. Ashtiani, A. J. Geers, and F. Aflatouni, “An on-chip photonic deep neural network for image classification,” Nature, vol. 606, no. 7914, pp. 501–506, Jun. 2022, doi: 10.1038/s41586-022-04714-0.

[7] S. Bandyopadhyay et al., “A Photonic Deep Neural Network Processor on a Single Chip with Optically Accelerated Training,” in CLEO 2023, San Jose, CA: Optica Publishing Group, 2023, p. SM2P.2. doi: 10.1364/CLEO_SI.2023.SM2P.2.

[8] J. Su and W. Chen, “A Microwave Photonic Frequency-Doubling Phase Shifter Based on Dual-Parallel Mach–Zehnder Modulators,” Photonics, vol. 11, no. 2, p. 116, Jan. 2024, doi: 10.3390/photonics11020116.

[9] H. Termos and A. Mansour, “Terahertz Replica Generation of Ultra-High Data Rate Transmission in an Electro-Optical Semiconductor Optical Amplifier Mach–Zehnder Interferometer System,” Photonics, vol. 11, no. 1, p. 83, Jan. 2024, doi: 10.3390/photonics11010083.

[10] Y. Gao et al., “Wideband Anti-interference Microwave Photonic Measurement for Doppler Frequency Shift and Angle of Arrival,” IEEE Trans. Instrum. Meas., pp. 1–1, 2024, doi: 10.1109/TIM.2024.3353871.

[11] J.-M. Lee et al., “Versatile Quantum State Generation and Manipulation in a Programmable Silicon-Photonic 4-Qubit System with High-Fidelity and Purity,” preprint, Dec. 2023. doi: 10.1364/opticaopen.24901572.v1.

[12] Y. Tang et al., “High-sensitivity displacement sensing based on an OEO incorporating an unbalanced MZI,” Optics & Laser Technology, vol. 121, p. 105816, Jan. 2020, doi: 10.1016/j.optlastec.2019.105816.

[13] A. M. Taha, S. Yousuf, M. S. Dahlem, and J. Viegas, “Highly-Sensitive Unbalanced MZI Gas Sensor Assisted With a Temperature-Reference Ring Resonator,” IEEE Photonics J., vol. 14, no. 6, pp. 1–9, Dec. 2022, doi: 10.1109/JPHOT.2022.3215713.

[14] R. B. Priti, G. Zhang, and O. Liboiron-Ladouceur, “3×10 Gb/s silicon three-mode switch with 120° hybrid based unbalanced Mach-Zehnder interferometer,” Opt. Express, vol. 27, no. 10, p. 14199, May 2019, doi: 10.1364/OE.27.014199.
[15] Z. Zou, J. Liu, L. Zhang, Z. Wang, and L. Zhan, “Temporal manipulation of light propagation via cross-intensity modulation in unbalanced fiber Mach-Zehnder interferometers,” Opt. Express, vol. 23, no. 23, p. 29584, Nov. 2015, doi: 10.1364/OE.23.029584.
[16] R. J. Bojko, J. Li, L. He, T. Baehr-Jones, M. Hochberg, and Y. Aida, “Electron beam lithography writing strategies for low loss, high confinement silicon optical waveguides,” Journal of Vacuum Science & Technology B, Nanotechnology and Microelectronics: Materials, Processing, Measurement, and Phenomena, vol. 29, no. 6, p. 06F309, Nov. 2011, doi: 10.1116/1.3653266.
[17] L. Chrostowski and M. Hochberg, Silicon photonics design: from devices to systems. Cambridge University Press, 2015.
[18] “Maple Leaf Photonics, Seattle WA, USA.” [Online]. Available: http://mapleleafphotonics.com
[19] M. Caverley, “Python code developed by Michael Caverley.” [Online]. Available: http://siepic.ubc.ca/probestation
[20] Y. Wang et al., “Focusing sub-wavelength grating couplers with low back reflections for rapid prototyping of silicon photonic circuits,” Opt. Express, vol. 22, no. 17, p. 20652, Aug. 2014, doi: 10.1364/OE.22.020652.